Magnetotactic bacteria form magnetite from a phosphate-rich ferric hydroxide via nanometric ferric (oxyhydr)oxide intermediates

Jens Baumgartner[a,1], Guillaume Morin[b], Nicolas Menguy[b], Teresa Perez Gonzalez[a], Marc Widdrat[a], Julie Cosmidis[b], and Damien Faivre[a]

[a]Department of Biomaterials, Max Planck Institute of Colloids and Interfaces, 14424 Potsdam, Germany; and [b]Institut de Minéralogie et de Physique des Milieux Condensés, Unité Mixte de Recherche 7590 Centre National de la Recherche Scientifique, Université Pierre et Marie Curie, Institut de Recherches pour le Développement, Campus Jussieu, 75005 Paris, France

Edited by Joanna Aizenberg, Harvard University, Cambridge, MA, and accepted by the Editorial Board August 1, 2013 (received for review April 15, 2013)

The iron oxide mineral magnetite (Fe_3O_4) is produced by various organisms to exploit magnetic and mechanical properties. Magnetotactic bacteria have become one of the best model organisms for studying magnetite biomineralization, as their genomes are sequenced and tools are available for their genetic manipulation. However, the chemical route by which magnetite is formed intracellularly within the so-called magnetosomes has remained a matter of debate. Here we used X-ray absorption spectroscopy at cryogenic temperatures and transmission electron microscopic imaging techniques to chemically characterize and spatially resolve the mechanism of biomineralization in those microorganisms. We show that magnetite forms through phase transformation from a highly disordered phosphate-rich ferric hydroxide phase, consistent with prokaryotic ferritins, via transient nanometric ferric (oxyhydr)oxide intermediates within the magnetosome organelle. This pathway remarkably resembles recent results on synthetic magnetite formation and bears a high similarity to suggested mineralization mechanisms in higher organisms.

ferrihydrite | geomagnetism | hematite | nanoparticles | precursors

The iron oxide mineral magnetite (Fe_3O_4) is biomineralized by various organisms that exploit its magnetic and mechanical properties to fulfill biological functions in these organisms (1). For example, the homing pigeon mineralizes magnetite in its beak as a sensor for the geomagnetic field to successfully navigate over long distances (2). Chitons, marine mollusks that feed on algae attached to rock, use magnetite-reinforced radula teeth to scrape their food from the rocks' surface (3, 4). However, the most abundant and widespread occurrence of biogenic magnetite is found in magnetotactic bacteria, a group of marine and freshwater organisms from different phyla that share the common characteristic of intracellular magnetite mineralization for geomagnetic navigation purposes (5, 6).

In general, magnetite is formed as ferrimagnetic single-domain nanoparticles in discrete vesicle compartments called magnetosomes aligned by a bundle of filaments along the cell axis of the bacteria. Number, size, and morphology of the crystals can vary between species to a large extent; however, these properties remain constant within different members of a single species (5, 6). The unique control exerted by the magnetotactic bacteria over the synthesis of magnetite nanoparticles also has brought about a great deal of interest from outside the biological community. In particular, understanding the underlying synthesis principles might provide materials chemistry with novel methods to control magnetite nanoparticle properties for a wide range of applications (7). As a result, the formation mechanism has been studied in recent years by various microbiological, genetic, and physicochemical methods (5, 6). However, despite tremendous advances, specifically in the understanding of the involved genes' and proteins' roles (8–12), essential knowledge about the actual iron chemistry in the mineralization of the particles lags behind. Characterization of the magnetite's precursor material is particularly critical for understanding different and crystallographically unusual nanoparticle morphologies. For example, ion-by-ion growth is expected to yield crystals with well-defined facets that are consistent with the underlying crystal structure; that is, uniform growth along energetically identical planes leading to cubo-octahedrally shaped magnetite particles. In contrast, organisms often make use of amorphous precursor phases, which can be molded into the desired morphology before crystallization (13). Beautiful examples of this phenomenon are found, for example, for magnetite in the chiton's teeth (4), for calcium carbonate in sea urchins (14, 15), and for calcium phosphate in bone (16). However, for magnetite in magnetotactic bacteria, this notion is not yet experimentally well supported, although often preferential anisotropic growth along one [111] direction is observed in some strains (17, 18). Furthermore, mechanisms of biogenic magnetite formation in general have remained elusive and are still under debate, in particular regarding the presence, nature, and localization of precursors (19–21). Magnetotactic bacteria can therefore serve as model systems, as the handling and genetic manipulation of bacterial cultures is straightforward with respect to studies on higher organisms such as, for example, the pigeon (2).

First attempts to characterize iron speciation in magnetotactic bacteria were made by Frankel et al. (19), who suggested three different phases in the magnetite crystallization process inferred from data obtained by Mössbauer spectroscopy on mature *Magnetospirillum magnetotacticum* strain MS-1: a low-density-hydrous ferric oxide that was followed by a high-density-hydrous ferric oxide (namely ferrihydrite [Fh]), which on partial reduction transforms to magnetite. However, spatiotemporal aspects remained unresolved. More recently, methods for the cultivation of magnetotactic bacteria in Fe-depleted media have enabled time-resolved experiments in which magnetite mineralization can be induced at will on the transfer of cells into Fe-containing media. Using this method, a Mössbauer study on *Magnetospirillum gryphiswaldense* strain MSR-1 (20) did not observe any mineral precursors apart from ferritin, from which, along with ferrous iron, magnetite was suggested to be coprecipitated inside the magnetosome compartments. However, the spatial information was inferred from cellular fractionation, not microscopy. On the

Author contributions: J.B., G.M., N.M., and D.F. designed research; J.B., G.M., N.M., T.P.G., M.W., and J.C. performed research; J.B., G.M., N.M., T.P.G., M.W., J.C., and D.F. analyzed data; and J.B., G.M., N.M., and D.F. wrote the paper.

The authors declare no conflict of interest.

This article is a PNAS Direct Submission. J.A. is a guest editor invited by the Editorial Board.

Freely available online through the PNAS open access option.

[1]To whom correspondence should be addressed. E-mail: jens.baumgartner@mpikg.mpg.de.

This article contains supporting information online at www.pnas.org/lookup/suppl/doi:10.1073/pnas.1307119110/-/DCSupplemental.

basis of X-ray circular magnetic dichroism, hematite (α-Fe_2O_3) was found as a precursor to magnetite in the same bacterial strain and was suggested to represent an outer layer around the nascent magnetite phase from which it grew (21). Very recently, the involvement of bacterioferritin in the mineralization pathway was again suggested in this strain (22). Thus, it remained to be determined which of the differently proposed precursor materials is involved in the mineralization of magnetite or how the different findings can be reconciled, how the precursors are spatially distributed within the bacterial cell, and how the phase transformation proceeds from precursor to final mineral.

Here we show that the magnetotactic bacterium *Magnetospirillum magneticum* strain AMB-1 forms a highly disordered, phosphate-rich ferric hydroxide phase consistent with prokaryotic ferritins, which transforms via nanometric ferric (oxyhydr)oxides to magnetosomal magnetite. We used Fe K-edge X-ray absorption spectroscopy at cryogenic temperatures to characterize the involved iron species and to investigate their time-resolved evolution. High-resolution transmission electron microscopy (HRTEM), high-angle annular dark-field scanning transmission electron microscopy (HAADF-STEM), and energy-dispersive X-ray spectroscopy (XEDS) mapping localize the magnetite precursor phase, as distributed discretely along the bacterial cell axis in agreement with the known chain structure of magnetosome vesicles indicating localization within these compartments. Position, size, and morphology of precursor and product support the notion of a solid-state phase transformation from nanometric ferric (oxyhydr) oxides comparable with recent observations of magnetite formation in solution (23) and biomineralization of other minerals in vivo (14–16).

Results and Discussion

The magnetotactic bacteria were initially grown in Fe-depleted aerobic medium to reach a nonmagnetic state. On cell transfer into microaerobic Fe-containing medium, both conventional bright-field TEM and magnetically induced differential light scattering coefficient (C_{mag}) assay (24), a qualitative test for bacterial orientation in a magnetic field, show the rapid accumulation of iron and formation of magnetite (Figs. S1–S5). TEM shows, after just 10 min, the first dark-contrasted spots of a few nanometers size in the cells, which form over time discretely and are widely distributed on a nearly linear axis along the inner curvature of the spirillum helix consistent with the known localization of the magnetosomes in AMB-1 (Fig. S3) (25). The onset of magnetic response ($C_{mag} > 0$) appears within 75–105 min (Fig. S1), in agreement with similar observations on *M. gryphiswaldense* MSR-1 (20).

We use the X-ray absorption near-edge structure (XANES) at the Fe K-edge to follow the iron speciation in samples collected and immediately frozen along the time-course experiment (Fig. 1). The characteristic spectral features of magnetite become increasingly dominant over time: an intensifying and narrowing 1s-3d/4p electron transition preedge peak at 7,114 eV (Fig. S6), which is in agreement with the increasing presence of tetrahedrally coordinated Fe^{3+} ions (26, 27), a shoulder feature in the edge at 7,127 eV, and strong peaks at 7,131 and 7,146 eV (Fig. 1*A*, black arrows). From the first to the last member in the time series, we observe a shift of the Fe edge toward lower energy values consistent with the increase of Fe^{II} in the magnetite structure ($Fe^{III}_2Fe^{II}O_4$; Fig. S6). This shift indicates an overall reductive phase formation process in vivo. At the early stages, we observe a shoulder feature at 7,139 eV (Fig. 1*A*, red arrow), which disappears concomitantly with the crystallization of magnetite. This shoulder is observed in the XANES spectrum of a regular Fe^{III} octahedron, such as the Fe^{III} hexaaquo complex, and in strengite ($FePO_4{\cdot}2H_2O$) (28). It is also observed in hydrated amorphous ferric sulfate (27), as well as in poorly ordered ferric phosphates (28).

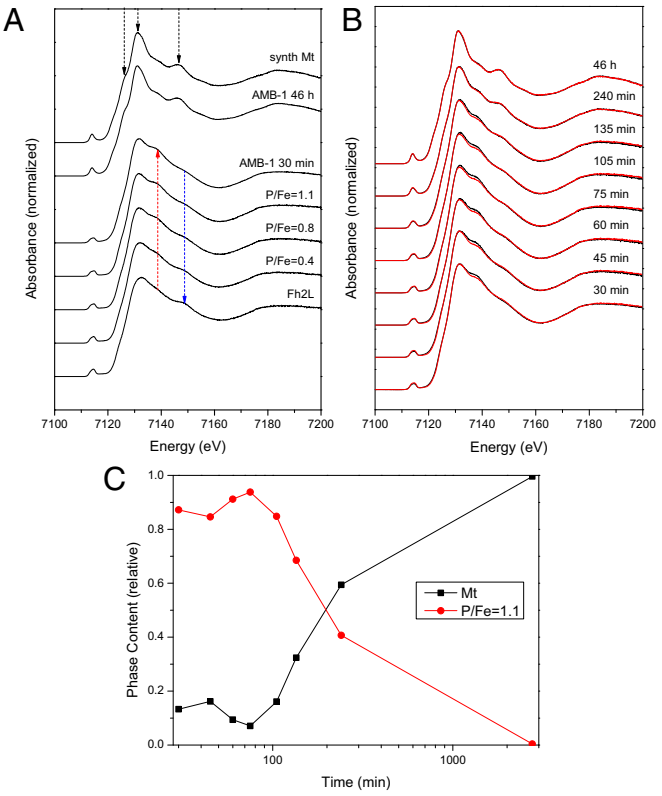

Fig. 1. Time-resolved mineralization of magnetite from a phosphate-rich ferric hydroxide compound (bacterioferritin) in *M. magneticum* AMB-1. (*A*) Comparison of bacterial and reference spectra. (*B*) High-resolution XANES of Fe-induction time-series: experimental data are plotted in black, and linear combination data are in red. (*C*) Relative iron phase content, as determined by linear combination fitting. P/Fe, phosphate-to-iron ratio; Synth Mt, synthetic magnetite; Fh2L, 2-line Fh.

It is known that prokaryotes can store iron in the form of (bacterio)ferritin, proteins that can contain large amounts of phosphate along with iron, which disturbs the mineral structure (29–31). Thus, we hypothesized a phosphate contribution to the bacterial iron species studied here, which is supported by the similarity between the spectrum of the early bacterial mineral and that of the poorly ordered ferric phosphate hydroxides we synthesized as model compounds. Accordingly, the shoulder is clearly observed in the XANES spectra of our poorly ordered ferric phosphate hydroxides, and its intensity increases with an increasing P/Fe ratio (P/Fe = 0.4, 0.8, and 1.1) (Fig. 1*A*). In contrast, the shoulder at 7,139 eV is not observed in Fh, the mineral usually associated with ferritin. In addition, the shoulder at 7,149 eV characteristic for Fh (blue arrow) almost completely disappears in our model phosphate compounds and the early-stage cells.

Linear combination fitting of the time-resolved induction series with the obtained standard spectra reveals that the bacteria, on the basis of XANES, contain only two major different pools of iron, which change their spectral contributions over the time-course of biomineralization (Fig. 1 *B* and *C* and Figs. S7–S9): a disordered ferric phosphate-like phase, similar to the P/Fe = 1.1 model compound, and the growing magnetite phase. Although the Fe K-edge jump intensity (which is proportional to the iron concentration) increased by three- to fourfold over the investigated time, the phase content of phosphate-rich ferric hydroxide dropped from around 90% to 0% (Fig. 1*C*). Thus, the concentration of the phosphate compound fell below its initial value, indicating that the material is consumed in the

mineralization of magnetite. Note also the remarkable correlation between the onsets of magnetic response in the C_{mag} assay and detectable magnetite in XANES (Fig. 1*C* and Fig. S1).

We analyze further the extended X-ray absorption fine structure (EXAFS) of the two involved major species: Fig. 2 shows the first- and second-shell fitting results of Fe in the late stage of induced cells after 46 h, which contain mainly mature magnetosomes, and the early stage after 30 min, devoid of mature magnetosomes (Fig. S2). Accordingly, for mature cells, we obtain a good-quality fit to the inverse spinel magnetite structure (Fig. 2 and Table S1). Note that in magnetite, two distinct iron sites exist, of which two-thirds are octahedrally and one-third are tetrahedrally coordinated (32). Respectively, we observe Fe-Fe paths at 2.97 and 3.47 Å. The Fe-O distances at 1.89 Å (coordination number [CN], 4) and 2.06 Å (CN, 6) cannot be separately resolved in our EXAFS measurements, but the fitted Fe-O distance is consistent with the weighted average of 2.02 Å expected from crystallographic data (32). In Fe-oxides containing both octahedrally and tetrahedrally coordinated iron (III), the out-of-phase interference between these two Fe-O shells

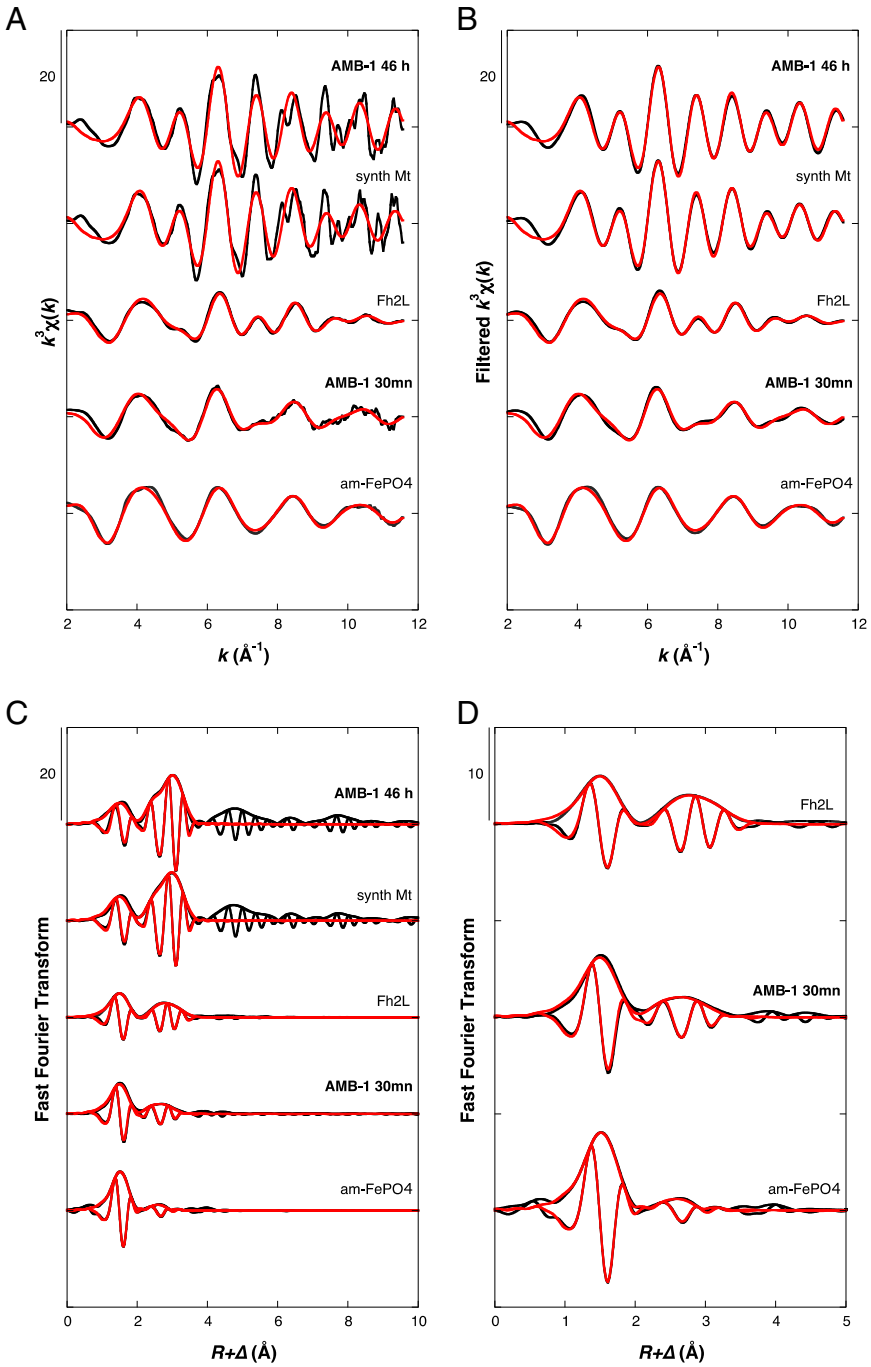

Fig. 2. Shell-by-shell fit of the EXAFS data recorded for mature and early mineralization stage AMB-1 plus model compounds. Experimental and calculated curves are plotted black and red, respectively. (*A*) Unfiltered EXAFS $k^3\chi(k)$ functions. (*B*) Fourier transform of unfiltered $k^3\chi(k)$ functions. (*C* and *D*) Fourier filtered $k^3\chi(k)$ functions within the 0–4-Å R-range.

systematically leads to an underestimation by EXAFS of the total number of first oxygen neighbors around the iron atom (n = 3.5–4.5) compared with that expected from crystal structure (e.g., n = 5.25–5.33 for maghemite and magnetite, respectively) (26). In the early mineralization stage, the second shell features in the Fourier Transform are much weaker than for mature cells (Fig. 2 *C* and *D*). Shell-by-shell fit of the AMB-1 30-min EXAFS data indicates that the material comprises octahedrally coordinated iron with oxygen in the first shell at a ∼2.00-Å distance. Second-shell paths include both Fe-Fe at ∼3.0 Å and Fe-P at 3.24 Å, in agreement with the structures of poorly ordered phosphate-containing ferric oxyhydroxides. In such phases, the linkage of phosphate tetrahedra to corners of the FeO_6 octahedra (Fe-P ∼3.25 Å) progressively suppresses the characteristic Fe-Fe interactions of the Fh structure at ∼3.45 Å and ∼3.0 Å (28), which are also present in horse spleen ferritin (29, 31). Hence, when increasing the P/Fe ratio, the interaction at ∼3.45 Å distance is the first to disappear, and the ∼3.0 Å distance is also absent in amorphous ferric phosphate, as illustrated by the EXAFS analysis of our model compound sample (am-$FePO_4$).

To locate the phosphate-rich ferric hydroxide phase within the cells, we studied the earliest mineralization stages, using HAADF-STEM and XEDS elemental mapping. For AMB-1 after 10 min induction, it appears that iron and phosphorus are spatially correlated in diffuse intracellular patches, in line with the observation of the disordered phosphate-rich ferric hydroxide phase by XANES and EXAFS (Fig. 3 *B* and *C*). Both methods reveal that iron, but not phosphorus, is also localized along the inner curvature of the helical cells in the form of defined nanometric particles or small aggregates, consistent with the dark contrasted objects observed by conventional bright-field TEM (Fig. S3). These particles and aggregates are distributed linearly along the long axis of the cell helix at discrete spacings of 76 ± 31 nm in agreement with the known location and size of the magnetosome compartments in AMB-1 (25). HRTEM and fast Fourier transform (FFT) analyses show that the earliest observed crystalline particles 10 min after induction are magnetite (∼50%) or nanometric ferric (oxyhydr) oxide aggregates (∼50%) such as Fh, poorly crystalline iron oxyhydroxides, and hematite (Fig. 3 *D*–*F* and Figs. S3 and S4). Particles of all phases at this stage fall within the same size range of around 8 ± 4 nm. Thirty minutes after induction, only magnetite particles were observed (Fig. S5).

Although Fh is known to be a metastable precursor of magnetite in the presence of ferrous iron, hematite is typically considered thermodynamically too stable. However, the high surface energy of 0.75 ± 0.16 $J \cdot m^{-2}$ renders the small and irregularly shaped nanohematite in the size range observed here with surface areas ≥∼26,000 $m^2 \cdot mol^{-1}$ (equivalent to a minimal surface ∼7-nm sphere) potentially as metastable as the Fh phase (33). Phosphate inhibits the formation of iron oxides including magnetite (34); thus, a biochemical mechanism must exist in the magnetotactic bacteria that is able to separate phosphate from the environment of the nascent magnetite phase in the magnetosome vesicles likely concomitant with transmembrane transport. In addition, the observed reduction of ferric to ferrous iron is consistent with typical biological redox potentials (35), although the specific physicochemical parameters within these vesicles are unknown.

Bacterioferritin has not been studied in detail by high-resolution imaging techniques because of its amorphous character. Eukaryotic ferritins, in contrast, are well-studied proteins and show structural features consistent with ∼5-nm large iron-containing particles with ∼2-nm-sized domains of Fh, and sometimes hematite, very similar to our observations in the bacteria (36, 37). Prokaryotic ferritin primarily differs from its eukaryotic homologs in its high-phosphate content, which can reach P/Fe ratios of

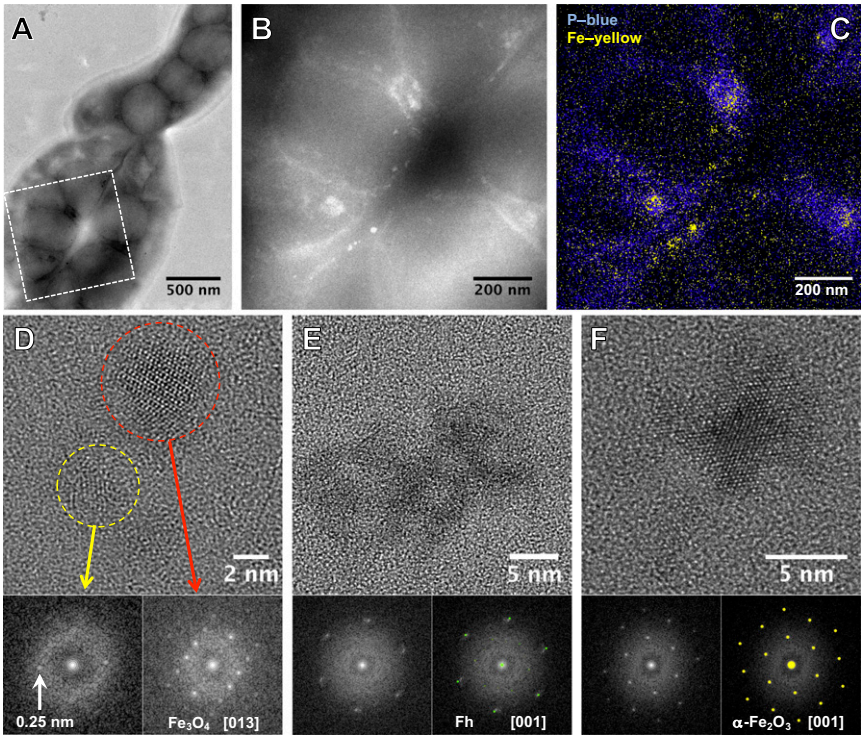

Fig. 3. TEM observations of AMB-1 at t = 10 min after induction. (*A*) Bright-field TEM image of a bacteria assembly. (*B*) HAADF-STEM image of the selected area in *A* revealing the presence of aggregates in the cell. (*C*) XEDS elemental mapping showing the colocalization of iron and phosphorus. (*D*–*F*) HREM observations of intracellular nanoparticles and their corresponding FFT analyses. (*D*) A magnetite nanocrystal is observed close to a poorly crystallized particle for which the interplanar distance of 0.25 nm is compatible with the Fh phase. (*E*) Poorly crystallized particle for which the diffraction is related to Fh. (*F*) Hematite nanoparticle.

1.7 (for comparison, horse spleen ferritin has a ratio of P/Fe of 0.125) (30). Therefore, we expect that separation of phosphate from bacterioferritin will lead to crystallization of Fh, as observed here within the magnetosomes (Fig. 4). On partial reduction of Fe^{III} to Fe^{II}, this nanometric phase can transform to magnetite. As we did not observe Fh by X-ray absorption spectroscopy, this phase is likely only present as minor and short-lived intermediate in this process. The irregular morphology of the first magnetite particles supports the notion of a solid-phase transformation from the precursor. In fact, only very recently have we been able to demonstrate that in solution, synthetic magnetite nucleates and grows from nanometric Fh-like aggregates bearing close resemblance to the precursor material here, both in size and morphology (23). Similarly, the precursor in the in vitro system is short-lived and does not form a bulk amorphous phase, as seen, for example, in $CaCO_3$. Although the bacterial strain investigated here does not show symmetry-breaking anisotropic crystal growth, as found in some strains, such as *Magnetococcus marinus* MC-1, *Magnetovibrio blakemorei* MV-1, or *Desulfovibrio magneticus* RS-1 (5), we expect that the mechanism observed here could enable such shape formation by the controlled deposition of the precursor inside the magnetosome compartments. We expect a suppression of the mineralization, as observed in several spontaneous and genetically modified mutants, when either phosphate separation or Fe^{III} reduction are impeded in the magnetosomes (5, 8–12). A particularly interesting case, and one potentially relevant to our observation of hematite in the early phase, is the report about a MamM mutant in *M. gryphiswaldense* MSR-1, which produces hematite containing magnetosomes by a mechanism that is yet unknown (9).

Conclusions

In conclusion, we show that magnetite formation in magnetotactic bacteria proceeds from a phosphate-rich ferric hydroxide phase, supposedly via a transient and short-lived Fh phase followed by reduction to form the final magnetite mineral (Fig. 4). The findings described here also bear significance beyond magnetite mineralization in magnetotactic bacteria alone, as some higher organisms such as the homing pigeon are also capable of its formation. Interestingly, in these birds, magnetite appears to be colocalized with ferric phosphate, suggesting potential similarities in the formation mechanisms in pro- and eukaryotes (38). Finally, we believe that the understanding of the process in the bacteria can lead to unique morphology-selective synthesis methods for magnetite nanoparticles and their future technological applications.

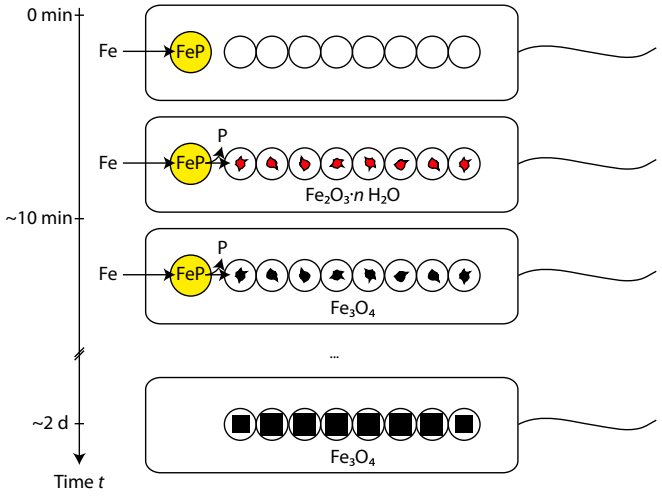

Fig. 4. Schematic illustration of the suggested magnetite biomineralization mechanism in magnetotactic bacteria. On uptake, iron (Fe) is stored in a phosphate-rich ferric hydroxide phase (FeP). Fe and P are separated in the transfer process into the magnetosome compartments, leading to the formation of Fh ($Fe_2O_3{\cdot}n\ H_2O$). Reduction of this phase yields magnetite, which grows out to mature crystals.

Materials and Methods

Bacterial Samples. *M. magneticum* (AMB-1) was grown aerobically at 28 °C in modified low iron medium, harvested and transferred to microaerobic (1% oxygen) flask standard medium (1.4 L) to induce magnetite biomineralization (39). Induced cells were sampled at consecutive times (90–135 mL each), centrifuged 5 min at 9,000 × *g*, 4 °C, and washed 3× with 5 mL Tris-buffered saline at pH 7.6. The pellets were resuspended in 100 μL Tris-buffered saline plus 25 μL glycerol and frozen in liquid nitrogen on sample holders with Kapton film support. Because iron concentrations in these samples did not exceed 0.1 $mol{\cdot}L^{-1}$, X-ray absorption spectroscopy (XAS) amplitude reduction resulting from self-absorption was expected to be less than 10%, as estimated using the algorithms implemented in Athena (40). Samples were stored at −80 °C and sent to European Synchrotron Radiation Facility on dry ice, where they were stored at −80 °C until measurement.

Synthetic Reference Samples. Synthetic samples were precipitated on-site, using a modified commercial titration device (Metrohm) equipped with an oxygen sensor (PreSens). Magnetite was precipitated under nitrogen atmosphere by slow dosing of a ferrous and ferric iron chloride solution (333 mM Fe^{II} and 667 mM Fe^{III} at a rate of 1 $\mu L{\cdot}min^{-1}$) to a dilute sodium hydroxide solution (10 mL) constantly kept at pH 9. Fh was precipitated by neutralization of a ferric nitrate solution (0.1 M) with sodium hydroxide. Ferric phosphate hydroxides were precipitated analogously after the addition of phosphoric acid with stoichiometries of P/Fe = 0.5, 1.0, and 1.5, yielding P/Fe = 0.4, 0.8, and 1.1 (±0.5) minerals, as determined by energy-dispersive X-ray spectroscopy. Samples (100 μL) were mixed with 25 μL glycerol and frozen in liquid nitrogen for XAS. An amorphous ferric phosphate hydroxide referred to as am-$Fe^{III}PO_4$ and analyzed previously using EXAFS spectroscopy at the SAMBA beamline (SOLEIL) was synthesized with an initial P/Fe ratio of 1.5, according to the procedure of Eynard et al. (41).

X-Ray Absorption Spectroscopy. Fe K-edge XANES spectra and EXAFS spectra were recorded at the undulator beamline ID26 of the European Synchrotron Radiation Facility. We used Si(311) double-crystal monochromator and focusing mirrors, giving a beam spot size of ~200 × 400 μm^2 on the samples. Data were recorded in fluorescence detection mode, using a Rowland-type spectrometer equipped with 4 Ge(440) analyzer crystals and a Si-photodiode. During all measurements, samples were cooled to 20 K, using a liquid He cryostat. Spectra were collected in quick-scan mode, scanning the undulator gap for EXAFS data. XANES spectra and preedge spectra were recorded with 0.1 eV step, counting 20 s from 7,100 to 7,200 eV and 30 s from 7,103 to 7,122 eV, respectively. EXAFS spectra were recorded up to k = 11.7 $Å^{-1}$, using 1 eV steps and counting for 300–500 s per scan. To improve data quality, 10–100 XANES scans and 10–60 EXAFS scans were recorded for each sample. Samples were moved a few hundred microns between each scan to minimize radiation damage. Data were averaged, using PyMca 4.6.0 (42), after evaluation for iron photo reduction. Averaged spectra were normalized using Athena 0.8.059 (40), and EXAFS data were extracted using the Autoback routine, using the same program. Linear combination fitting of XANES data were performed with the respective functions of Athena. EXAFS data were Fourier Transformed over the k = 2–11.6 $Å^{-1}$ range, applying a Kaiser-Bessel window with a Bessel-weight of 2.5. Nonfiltered and filtered (0–4Å R-range, uncorrected for phase shift) EXAFS data were fit in k-space, with an amplitude reduction parameter S_0^2 (32) set to a value of 1 (26). Phase and amplitude functions used in this procedure were calculated with Feff8 (43), according to curve-wave backscattering theory of EXAFS and using the magnetite crystal structure of Fleet (32) and the vivianite structure of Fejdi (44).

Electron Microscopy. Samples were adsorbed to carbon film-coated Cu TEM grids. After removal of the liquid with Kimwipe paper, grids were washed with a drop of deionized water to remove residual salt precipitates. Standard imaging was performed on a Zeiss EM 912 Omega with 120 kV acceleration voltage. HRTEM, HAADF-STEM, and XEDS elemental mapping was carried out on a Jeol 2100F microscope. This machine, operating at 200 kV, is equipped with a field emission gun, an ultra-high-resolution pole piece, and an ultrathin window JEOL detector. HRTEM images were obtained with a Gatan US 4000 CCD camera.

X-Ray Diffraction. Reference samples (Fig. S9) were studied at the μSpot beamline of BESSY II, using a Si 111 double-crystal monochromator-defined 100-μm-wide beam of 15 keV. Diffraction data were acquired on a 3,072 × 3,072 pixel MarMosaic 225 CCD camera (Mar USA) with a 73.242-μm pixel size. The sample-detector distance was determined from an internal or external α-SiO_2 standard. Data reduction was performed using Fit2D.

ACKNOWLEDGMENTS. We thank J.-D. Cafun, P. Glatzel, and C. Lapras for assistance in using beamline ID26 (European Synchrotron Radiation Facility); L. Bertinetti for EDX on reference compounds and S. Siegel and C. Li (μSpot beamline of BESSY II, Helmholtz Zentrum Berlin); and Y. Politi for discussion on the manuscript. We acknowledge the European Synchrotron Radiation Facility for provision of synchrotron radiation facilities. The research was supported by the Max Planck Society and the European Research Council through Starting Grant 256915-MB2 (to D.F.).

1. Kirschvink JL, Walker MM, Diebel CE (2001) Magnetite-based magnetoreception. *Curr Opin Neurobiol* 11(4):462–467.
2. Mora CV, Davison M, Wild JM, Walker MM (2004) Magnetoreception and its trigeminal mediation in the homing pigeon. *Nature* 432(7016):508–511.
3. Gordon LM, Joester D (2011) Nanoscale chemical tomography of buried organic-inorganic interfaces in the chiton tooth. *Nature* 469(7329):194–197.
4. Lowenstam HA (1967) Lepidocrocite, an apatite mineral, and magnetic in teeth of chitons (Polyplacophora). *Science* 156(3780):1373–1375.
5. Faivre D, Schüler D (2008) Magnetotactic bacteria and magnetosomes. *Chem Rev* 108(11):4875–4898.
6. Komeili A (2012) Molecular mechanisms of compartmentalization and biomineralization in magnetotactic bacteria. *FEMS Microbiol Rev* 36(1):232–255.
7. Baumgartner J, Faivre D (2011) Magnetite biomineralization. *Molecular Biomineralization. Progress in Molecular and Subcellular Biology*, ed Müller WEG (Springer, Heidelberg), Vol 52, pp 3–27.
8. Murat D, Quinlan A, Vali H, Komeili A (2010) Comprehensive genetic dissection of the magnetosome gene island reveals the step-wise assembly of a prokaryotic organelle. *Proc Natl Acad Sci USA* 107(12):5593–5598.
9. Uebe R, et al. (2011) The cation diffusion facilitator proteins MamB and MamM of Magnetospirillum gryphiswaldense have distinct and complex functions, and are involved in magnetite biomineralization and magnetosome membrane assembly. *Mol Microbiol* 82(4):818–835.
10. Murat D, et al. (2012) The magnetosome membrane protein, MmsF, is a major regulator of magnetite biomineralization in Magnetospirillum magneticum AMB-1. *Mol Microbiol* 85(4):684–699.
11. Lohsse A, et al. (2011) Functional analysis of the magnetosome island in *Magnetospirillum gryphiswaldense*: The *mamAB* operon is sufficient for magnetite biomineralization. *PLoS ONE* 6(10):e25561.
12. Tanaka M, Mazuyama E, Arakaki A, Matsunaga T (2011) MMS6 protein regulates crystal morphology during nano-sized magnetite biomineralization in vivo. *J Biol Chem* 286(8):6386–6392.
13. Weiner S, Addadi L (2011) Crystallization Pathways in Biomineralization. *Annu Rev Mater Sci* 41(1):21–40.
14. Politi Y, Arad T, Klein E, Weiner S, Addadi L (2004) Sea urchin spine calcite forms via a transient amorphous calcium carbonate phase. *Science* 306(5699):1161–1164.
15. Seto J, et al. (2012) Structure-property relationships of a biological mesocrystal in the adult sea urchin spine. *Proc Natl Acad Sci USA* 109(10):3699–3704.
16. Mahamid J, et al. (2010) Mapping amorphous calcium phosphate transformation into crystalline mineral from the cell to the bone in zebrafish fin rays. *Proc Natl Acad Sci USA* 107(14):6316–6321.
17. Devouard B, et al. (1998) Magnetite from magnetotactic bacteria: Size distributions and twinning. *Am Mineral* 83:1387–1398.
18. Lefèvre CT, et al. (2011) Morphological features of elongated-anisotropic magnetosome crystals in magnetotactic bacteria of the Nitrospirae phylum and the Deltaproteobacteria class. *Earth Planet Sci Lett* 312(1-2):194–200.
19. Frankel RB, Papaefthymiou GC, Blakemore RP, O'Brien W (1983) Fe_3O_4 Precipitation in Magnetotactic Bacteria. *Biochim Biophys Acta* 763:147–159.
20. Faivre D, Böttger LH, Matzanke BF, Schüler D (2007) Intracellular magnetite biomineralization in bacteria proceeds by a distinct pathway involving membrane-bound ferritin and an iron(II) species. *Angew Chem Int Ed Engl* 46(44):8495–8499.
21. Staniland S, Ward B, Harrison A, van der Laan G, Telling N (2007) Rapid magnetosome formation shown by real-time x-ray magnetic circular dichroism. *Proc Natl Acad Sci USA* 104(49):19524–19528.
22. Fdez-Gubieda ML, et al. (2013) Magnetite biomineralization in Magnetospirillum gryphiswaldense: Time-resolved magnetic and structural studies. *ACS Nano* 7(4):3297–3305.
23. Baumgartner J, et al. (2013) Nucleation and growth of magnetite from solution. *Nat Mater* 12(4):310–314.
24. Schüler D, Uhl R, Baeuerlein E (1995) A simple light scattering method to assay magnetism in *Magnetospirillum gryphiswaldense*. *FEMS Microbiol Lett* 132:139–145.
25. Komeili A, Li Z, Newman DK, Jensen GJ (2006) Magnetosomes are cell membrane invaginations organized by the actin-like protein MamK. *Science* 311(5758):242–245.
26. Maillot F, et al. (2011) New insight into the structure of nanocrystalline ferrihydrite: EXAFS evidence for tetrahedrally coordinated iron(III). *Geochim Cosmochim Acta* 75(10):2708–2720.
27. Wilke M, Farges F, Petit P-E, Brown GE, Martin F (2001) Oxidation state and coordination of Fe in minerals: An Fe K-XANES spectroscopic study. *Am Mineral* 86(5-6):714–730.
28. Voegelin A, Kaegi R, Frommer J, Vantelon D, Hug SJ (2010) Effect of phosphate, silicate, and Ca on Fe(III)-precipitates formed in aerated Fe(II)- and As(III)-containing water studied by X-ray absorption spectroscopy. *Geochim Cosmochim Acta* 74(1):164–186.
29. Rose J, Manceau A, Bottero J-Y, Masion A, Garcia F (1996) Nucleation and Growth Mechanisms of Fe Oxyhydroxide in the Presence of PO_4 Ions. 1. Fe K-Edge EXAFS Study. *Langmuir* 12(26):6701–6707.
30. Rohrer JS, Islam QT, Watt GD, Sayers DE, Theil EC (1990) Iron environment in ferritin with large amounts of phosphate, from Azotobacter vinelandii and horse spleen, analyzed using extended X-ray absorption fine structure (EXAFS). *Biochemistry* 29(1):259–264.
31. Waldo GS, et al. (1995) Formation of the ferritin iron mineral occurs in plastids. *Plant Physiol* 109(3):797–802.
32. Fleet ME (1986) The structure of magnetite: Symmetry of cubic spinels. *J Solid State Chem* 62(1):75–82.
33. Navrotsky A, Mazeina L, Majzlan J (2008) Size-driven structural and thermodynamic complexity in iron oxides. *Science* 319(5870):1635–1638.
34. Borch T, Masue Y, Kukkadapu RK, Fendorf S (2007) Phosphate imposed limitations on biological reduction and alteration of ferrihydrite. *Environ Sci Technol* 41(1):166–172.
35. Kemp M, Go Y-M, Jones DP (2008) Nonequilibrium thermodynamics of thiol/disulfide redox systems: A perspective on redox systems biology. *Free Radic Biol Med* 44(6):921–937.
36. Quintana C, Cowley JM, Marhic C (2004) Electron nanodiffraction and high-resolution electron microscopy studies of the structure and composition of physiological and pathological ferritin. *J Struct Biol* 147(2):166–178.
37. Pan YH, et al. (2009) 3D morphology of the human hepatic ferritin mineral core: New evidence for a subunit structure revealed by single particle analysis of HAADF-STEM images. *J Struct Biol* 166(1):22–31.
38. Fleissner G, et al. (2003) Ultrastructural analysis of a putative magnetoreceptor in the beak of homing pigeons. *J Comp Neurol* 458(4):350–360.
39. Faivre D, Menguy N, Pósfai M, Schüler D (2008) Environmental parameters affect the physical properties of fast-growing magnetosomes. *Am Mineral* 93:463–469.
40. Ravel B, Newville M (2005) ATHENA, ARTEMIS, HEPHAESTUS: Data analysis for X-ray absorption spectroscopy using IFEFFIT. *J Synchrotron Radiat* 12(Pt 4):537–541.
41. Eynard A, Delcampillo MC, Barron V, Torrent J (1992) Use of vivianite ($Fe_3(PO_4)_2{\cdot}8H_2O$) to prevent iron chlorosis in calcareous soils. *Fert Res* 31(1):61–67.
42. Solé VA, Papillon E, Cotte M, Walter P, Susini J (2007) A multiplatform code for the analysis of energy-dispersive X-ray fluorescence spectra. *Spectrochim. Acta B* 62(1):63–68.
43. Ankudinov AL, Ravel B, Rehr JJ, Conradson SD (1998) Real-space multiple-scattering calculation and interpretation of x-ray-absorption near-edge structure. *Phys Rev B* 58(12):7565–7576.
44. Fejdi P, Poullen JF, Gasperin M (1980) Refinement of the structure of vivianite, $Fe_3(PO_4)_2{\cdot}8\ H_2O$. *Bull Mineral (Paris)* 103(1):135–138.